Key Points:
- A new version of the open-source Global Airglow (GLOW) model is released
- New features include selected far ultraviolet emissions, interfaces to general circulation models, and parallel processing
- Comparison with far ultraviolet limb scan measurements shows reasonable agreement

Correspondence to:
S. C. Solomon,
stans@ucar.edu

Global modeling of thermospheric airglow in the far ultraviolet

Stanley C. Solomon[1] (ID)

[1]High Altitude Observatory, National Center for Atmospheric Research, Boulder, Colorado, USA

Abstract The Global Airglow (GLOW) model has been updated and extended to calculate thermospheric emissions in the far ultraviolet, including sources from daytime photoelectron-driven processes, nighttime recombination radiation, and auroral excitation. It can be run using inputs from empirical models of the neutral atmosphere and ionosphere or from numerical general circulation models of the coupled ionosphere-thermosphere system. It uses a solar flux module, photoelectron generation routine, and the Nagy-Banks two-stream electron transport algorithm to simultaneously handle energetic electron distributions from photon and auroral electron sources. It contains an ion-neutral chemistry module that calculates excited and ionized species densities and the resulting airglow volume emission rates. This paper describes the inputs, algorithms, and code structure of the model and demonstrates example outputs for daytime and auroral cases. Simulations of far ultraviolet emissions by the atomic oxygen doublet at 135.6 nm and the molecular nitrogen Lyman-Birge-Hopfield bands, as viewed from geostationary orbit, are shown, and model calculations are compared to limb-scan observations by the Global Ultraviolet Imager on the TIMED satellite. The GLOW model code is provided to the community through an open-source academic research license.

Plain Language Summary The Global Airglow (GLOW) model has been updated and extended to calculate ultraviolet light emitted by the upper atmosphere, including during the day, during the night, and in the aurora. It can be run using inputs from standard climatological models of the upper atmosphere and ionosphere or from complex computer models that describe the dynamics of the ionosphere. It computes energetic electron fluxes from both solar and auroral sources, and it contains a chemistry module that calculates the densities of excited and ionized atoms and molecules, and the resulting airglow emission rates. This paper describes the inputs, algorithms, and code structure of the model and demonstrates example outputs for daytime and the aurora. Simulations of ultraviolet emissions by atomic oxygen and molecular nitrogen, as viewed from geostationary orbit, are shown, and model calculations are compared to observations by the Global Ultraviolet Imager on the TIMED satellite. The GLOW model code is provided to the community through an open-source academic research license.

1. Introduction

The terrestrial upper atmosphere emits light at discrete wavelengths throughout the spectrum, known collectively as airglow, but often referred to as dayglow, nightglow, and aurora, for different locations and excitation mechanisms. These emissions can be used in remote sensing of the upper atmosphere and ionosphere, provided that an accurate description of their production and loss mechanisms is obtained. The purpose of the Global Airglow (GLOW) model is to unify the physical and numerical descriptions of these various processes and apply them globally, in order to simulate observable emissions, and to make that model available to the aeronomy community.

Early versions of the GLOW model date back to work by *Solomon* [1987], *Solomon et al.* [1988], and *Solomon and Abreu* [1989], primarily concerned with the 630 nm "red line" emission of atomic oxygen. The approach used there for auroral and dayglow energetic electron processes and chemistry was generalized to handle other visible-region emissions; later developments for use with odd-nitrogen chemistry are described by *Bailey et al.* [2002]. A version codified as v. 0.97 was released in 2005; this version and extensions were used in work by, e.g., *Solomon and Qian* [2005], *Doe et al.* [2005], *Solomon* [2006], *Smithtro and Solomon* [2008], *Tian et al.* [2008], *Peterson et al.* [2009, 2012], *McGranaghan et al.* [2015a,b], and *Kaeppler et al.* [2015]. During 2016–2017, a new version was developed with the goals of modernizing the code, interfacing seamlessly with output from general circulation models, implementing parallel processing, improving interoperability, and including ultraviolet emission features. This version, designated v. 0.98, is not intended to have large scientific changes from v. 0.97 but is released with the intent of establishing a more modern computational framework for future developments.

One of the goals of the code modernization is to operate on output from general circulation models such as the National Center for Atmospheric Research (NCAR) Thermosphere-Ionosphere-Electrodynamics General Circulation Model (TIE-GCM) [*Roble et al.*, 1988; *Richmond et al.*, 1992; *Qian et al.*, 2014] and similar models, in a parallel environment, including on supercomputers. This is done using standard netCDF files for input and output, and so is easily extensible to other general circulation models. The ability to run GLOW using empirical model inputs is also retained.

The most important new feature of GLOW is inclusion of selected emission features in the far ultraviolet, including the Lyman-Birge-Hopfield (LBH) bands of molecular nitrogen and the atomic oxygen doublet at 135.6 nm. These were implicitly included in the code previously, because their upper state populations are calculated, but they have now been included in output arrays, and initial validation has been conducted. The atomic oxygen 130.4 nm triplet is also output as excitation rates, but this optically thick feature is subject to high multiple scattering that is beyond the scope of this paper. The 135.6 nm emission is also subject to some scattering; a simple radiative transfer algorithm is employed in post-processing to deal with this effect.

2. Model Description

GLOW is a single-column, single-time model that can be run repeatedly to build up a global map and/or time history. It operates on specified thermospheric parameters with energetic inputs from the Sun and aurora. It computes ionization, dissociation, and excitation rates; performs energetic electron transport calculations; applies ion-neutral chemistry; and outputs ionized/excited species densities and airglow emission rates. This section provides a description of model inputs, methodology, implementation, and output.

2.1. Inputs
2.1.1. Solar Irradiance
The standard solar extreme ultraviolet (EUV) irradiance input to the NCAR TIE-GCM is provided by the EUV for Aeronomic Calculations (EUVAC) proxy model [*Richards et al.*, 1994, 2006]. For implementation in GLOW, EUVAC is binned into 1 nm spectral bands from 5 to 105 nm. Individual bands of the solar EUV photon flux are calculated by EUVAC as linear functions of the input variable P, which is defined as the average of the daily $F_{10.7}$ and its running 81 day centered mean. The model is extended below 5 nm using various historical measurements, as described in *Solomon and Qian* [2005]. The older *Hinteregger et al.* [1981] model is also included as an option, similarly binned at 1 nm resolution. Because of continuing controversies involving solar irradiance and its variability in the "XUV" region from ~1 to ~25 nm [cf., *Buonsanto et al.*, 1992, 1995; *Solomon et al.*, 2001; *Solomon*, 2006], a multiplicative factor may be specified to scale part of the solar spectrum upward (or downward); this factor is applied from 1.8 to 5 nm in the case of EUVAC and from 1.8 to 25 nm in the case of the Hinteregger model. Other solar irradiance models may also be employed.

Far ultraviolet (FUV) irradiances are provided by the *Woods and Rottman* [2002] model, which is based on data from the Upper Atmosphere Research Satellite. This model also employs daily $F_{10.7}$ and its 81 day mean to scale the solar irradiance. Five-nanometer bins are used from 105 to 175 nm, except that the H Ly α line at 121.6 nm has its own bin.

A measured solar flux may be used as input, provided that it is specified in the 123 bins used by GLOW throughout the range 0.05 to 175 nm. For example, data from the Solar EUV Experiment on the TIMED satellite [*Woods et al.*, 2005] and from the EUV Variability Experiment (EVE) on the Solar Dynamics Observatory (SDO) [*Woods et al.*, 2011] have been employed. This is handled through a simple file-based input. Any other model solar spectrum can similarly be used as input by binning it to the GLOW specification and writing a file for the particular date/time in a standard format. This can be either a daily average or time-specific spectrum, e.g., for flare studies.

2.1.2. Auroral Inputs
Auroral electron precipitation is applied by specifying a characteristic energy and total energy flux, which are used to generate a Maxwellian spectrum. An optional low-energy tail of the form given by *Meier et al.* [1989] may be included. Alternatively, a monoenergetic auroral electron flux may be specified. In either case, the auroral flux is assumed to be isotropic in pitch angle over the downward hemisphere, and the energy flux is given in power per unit area; i.e., it is a hemispherical flux that has been integrated with respect to the downward component of solid angle, equal to $\pi\Phi$, where Φ is an isotropic flux in units of erg cm^{-2} s^{-1} str^{-1}.

It is also possible to input an arbitrary measured or model spectrum by directly populating each energy bin of the "phitop" array with electron number fluxes ($cm^{-2}\ s^{-1}\ eV^{-1}$).

When running using TIE-GCM output, the characteristic energy and total energy flux used for the auroral oval are passed to GLOW as 2D fields, and used as spatially varying input to each column [*Solomon et al.*, 2012]. (The TIE-GCM uses the same inputs for auroral specification but employs a simple parameterized ionization rate profile rather than full electron transport.)

Proton and other ion precipitation are not currently included, although a proton transport model has been previously developed [*Solomon*, 2001] and used to produce a simplified parameterization [*Fang et al.*, 2013] that will be incorporated into the GLOW framework.

2.1.3. Neutral Atmosphere

GLOW makes no calculations of the major atmospheric gases N_2, O_2, and O; these, and the neutral temperature T_n, must be provided as inputs. Nitric oxide (NO) and ground-state atomic nitrogen (N(^{4}S)) must also be provided as inputs. Excited atomic nitrogen in the ^{2}D state is calculated by the model but may be provided as an optional input for initialization. When using the TIE-GCM, these are obtained globally from output history files. The interface routine also includes an option for obtaining these fields from the NCAR Thermosphere-Ionosphere-Mesosphere-Electrodynamics General Circulation Model [*Roble and Ridley*, 1994], and input from either model is supported in both high-resolution (2.5° horizontal and H/4 vertical) and low-resolution (5° horizontal and H/2 vertical) modes, where H is the pressure scale height. For altitudes below the ~97 km lower boundary of the TIE-GCM, simple exponential extrapolation of N_2 and O_2 is performed, O is exponentially decreased, and the odd-nitrogen species are assumed constant. This is only for purposes of providing a "sponge" layer for electron transport calculations; the model range of validity does not extend below 97 km when running with the TIE-GCM. Any other GCM input could be employed by appropriate modification of the input routines.

Empirical model inputs can also be used for N_2, O_2, O, and N(^{4}S). The drivers provided with the model package use the standard Naval Research Laboratory Mass Spectrometer Incoherent Scatter (NRLMSISE-00) atmosphere [*Picone et al.*, 2002]. Any other model or measurement could be substituted by modifying the driver or providing a file-based specification. For nitric oxide, an interface is provided to the Nitric Oxide Empirical Model (NOEM) [*Marsh et al.*, 2004], which is based on a climatological analysis of data from the Student Nitric Oxide Explorer (SNOE) satellite [*Solomon et al.*, 1996; *Barth et al.*, 2003].

2.1.4. Ambient Ionosphere

Electron density [e$^-$] is calculated by GLOW in the photochemically controlled region below ~200 km altitude, and ion composition is calculated at all altitudes, but no dynamical calculations are performed. Below ~200 km altitude, this is an acceptable approximation, but in the F region ionosphere above ~200 km, the ion and electron density are controlled by dynamical transport due to electric fields, neutral winds, and ambipolar diffusion, primarily acting on the atomic oxygen ion O$^+$. Also, for stability of the electron transport algorithm, there must be a nonzero electron density at all altitudes. Therefore, an electron density profile must be specified on input. Ion and electron temperatures T_i and T_e are also required. When running with GCM output, the global fields [e$^-$], T_i, and T_e, calculated by the GCM are utilized. Below 200 km, [e$^-$] is recalculated in the chemistry routine; above 200 km the input [e$^-$] is not changed. Both the input and calculated [e$^-$] are output. When using empirical model inputs, a version of the International Reference Ionosphere (IRI-90) [*Bilitza*, 1990] is provided with the driver routines. Although not the latest version of IRI, this is used for simplicity, since only the F region portion is employed, which is similar to more recent updates. As with the neutral atmosphere, any other empirical ionosphere model or measurement could be utilized.

Table 1 provides a summary of required and optional inputs and outputs.

2.2. Methods
2.2.1. Coordinate Systems

GLOW operates on individual columns in a geometric altitude space, with nominal altitude range from 80 km to ~600 km. There is no communication between columns. GLOW can be implemented in single-column mode, one column at a time, or run globally on a horizontal grid. When running from GCM fields, that grid is generally specified by the GCM. When running using empirical model inputs,

Table 1. Summary of Inputs and Outputs

Category	Geophysical	State Variables	Production Rate	Emission Rates
Required inputs	Date, UT, latitude, longitude	O, O_2, N_2, NO, $N(^4S)$, T_n, T_i, T_e, $[e^-]$		
Optional inputs	$F_{10.7}$, $<F_{10.7}>$	$N(^2D)$, O^+, O_2^+, NO^+, N_2^+, N^+	Solar EUV and FUV, auroral electron flux	
Standard outputs	Solar zenith angle, local solar time, magnetic inclination (dip) angle	$O^+(^2P)$, $O^+(^2D)$, $O^+(^4S)$, N^+, N_2^+, O_2^+, NO^+, $N(^2P)$, $N(^2D)$, $N_2(A)$, $O(^1S)$, $O(1D)$, $[e^-]$ (input), $[e^-]$ (calculated), σ_{ped}, σ_{hall}	Total ionization, species-specific photoionization, species-specific electron impact ionization	$N2(C)$ $2P(0,0)$ 337.1, $N_2^+(B)$ $1N(0,1)$ 427.8, $N(^2D)$ 520.0, $O(^1S)$ 557.7, $O(^1D)$ 630.0, $O^+(^2P)$ 732.0, $N(^2P)$ 1040.0, $N(^2P)$ 346.6, $O(3p^5P)$ 777.4, $O(3p^3P)$ 844.6, $O^+(^2D)$ 372.6, $N_2(a)$ LBH system, $O(3s^5S)$ 135.6, $N(3s^2P)$ 149.3, $O(3s^3S)$ 130.4
Available outputs		Electron impact cross sections	Photoelectron production, energetic electron flux, state-specific photoionization, photodissociation, electron impact ionization and electron impact excitation, electron heating	Solar irradiance, individual components of airglow emissions, vertical column brightnesses

any horizontal grid can be employed. For GCM input, the log-pressure coordinate system (in intervals of $H/4$) of the GCM is employed but translated to the corresponding geometric altitude. For empirical model inputs, an altitude grid is specified, using approximately $H/4$ spacing. For stability, it is inadvisable to use a coarser altitude grid.

The magnetic inclination or "dip angle" for electron transport calculations is calculated using an eccentric-dipole approximation adapted from the IRI-90 package. An eccentric-dipole approximation is also used to translate from geographic location to the geomagnetic latitude used in NOEM, similar to the method used to generate the zonal-mean SNOE data which is its basis.

2.2.2. Solar Irradiance Attenuation

The solar spectral irradiance described in section 2.1.1 above is applied to the upper boundary of the model and then propagated throughout the model column to all altitudes z in every wavelength bin λ through application of Beer's law:

$$I(z,\lambda) = I(\infty, \lambda)\, e^{-\tau(z,\lambda)} \qquad (1)$$

where the optical depth τ is calculated by summing the product of the total absorption cross sections σ and slant column density N for each of the three major species N_2, O_2, and O:

$$\tau(z,\lambda) = \Sigma_i \sigma_i(\lambda) N_i(z,\chi). \qquad (2)$$

The solar zenith angle χ is calculated for the date, time, and location of the model column. The slant column density is then calculated for each species by integrating its density from each altitude to the top of the model to obtain the vertical column density, and then multiplying by the Chapman grazing incidence integral function [*Chapman*, 1931]. This function (approximately equal to $1/\cos\chi$ for $\chi < \sim 60°$) accounts for the spherical geometry of the atmosphere and is estimated using a polynomial expansion [*Smith and Smith*, 1972]. For $\chi > 90°$,

$$N_i(z) = 2N_i(z_{tan}, 90°) - N_i(z, 180° - \chi) \qquad (3)$$

where z_{tan} is the tangent altitude of the solar vector.

2.2.3. Photoionization, Photodissociation, and Production of Photoelectrons

Once the attenuated solar spectral irradiance has been calculated at every altitude and wavelength, the state-specific rates for ionized states of each species are calculated, including dissociative ionization. Total cross sections are taken from the *Fennelly and Torr* [1992] compilation and from *Henke et al.* [1993] in the soft X-ray region. Branching ratios are from *Conway* [1988]. The production rates for each state at every altitude are then calculated by integrating over wavelength. Total photodissociation rates

are calculated by integrating over wavelength and state-specific photodissociation rates obtained by applying branching ratios.

Photoelectron production is embedded in this procedure. For every ionizing process in every wavelength bin, the ionization energy loss (including dissociation and excitation, if any) is subtracted from the photon energy. It is assumed that this remaining energy is entirely transferred to the photoelectron ejected in the ionization event. This neglects small amounts of kinetic energy residing in dissociated products and possibly vibrational/rotational energy of molecular ions. An electron energy grid consisting of 190 bins extending from 0 to 50 keV is defined using an expanding logarithmic scale; this grid is extensible for high-energy calculations, but the default range is sufficient for photoelectron and most auroral electron calculations. The photoelectron production rates from each solar wavelength are summed into the bins defined by the energy grid. Auger electrons produced by k-shell ionization are added for soft X-rays with sufficient energy (~500 eV for O and O_2 and ~360 eV for N_2; see *Bailey et al.* [2002] for details). All photoelectron production is assumed to be isotropic with respect to pitch angle.

An additional routine provides the background or nighttime ionization due to geocoronal emissions of hydrogen and helium that weakly ionize the *E* region and lower *F* region. The same simple formulation used in the TIE-GCM is employed, for consistency. This is applied uniformly over the globe, but is a negligible contribution to daytime ionization.

2.2.4. Electron Transport

At the heart of the GLOW model is the two-stream energetic electron transport algorithm originally designed by A. F. Nagy and P. M. Banks [*Nagy and Banks*, 1970; *Banks and Nagy*, 1970; *Banks et al.*, 1974] and implemented in a variety of ways by numerous developers, including for other planets. Additional descriptions of how the method is implemented in the GLOW model may be found in *Solomon* [1987], *Solomon et al.* [1988], and *Bailey et al.* [2002].

The principle of the two-stream algorithm is that an instantaneous energetic electron flux can be characterized by the two components (upward and downward) of its direction along a magnetic field line. Electrons are generally confined to spiral motions around the magnetic field line by electromagnetic forces, and in general, there is an arbitrary pitch angle distribution over 4π str. In a multistream numerical model, several pitch angle bins are used in both upward and downward directions; in the two-stream formulation, this is reduced to two, each with a characteristic pitch angle assumed to be ±60° to the magnetic field line. The path length ds through each atmospheric layer dz is

$$ds = dz/(\cos\xi \sin\delta) \tag{4}$$

where ξ is the characteristic pitch angle and δ is the inclination of the magnetic field to the horizontal. This approach is an excellent approximation for photoelectron calculations below the exobase, where pitch angle distributions are nearly isotropic in each hemisphere, but clearly has limitations when applied to auroral fluxes that can have highly anisotropic pitch angle distributions. However, the altitude of peak auroral ionization is not very sensitive to initial pitch angle distribution, because electromagnetic pitch angle redistribution and elastic scattering rapidly flatten any anisotropy as electrons enter the upper atmosphere, as shown by *Solomon* [2001], and the secondary electron flux is largely isotropic.

The boundary condition at the top of the atmosphere is an applied downward flux, either an auroral flux as described above or a plasmaspheric input flux, such as might be generated at by photoionization at the other end of the field line, or zero. The boundary condition at the bottom of the model is that the upward flux ϕ^+ equals the downward flux ϕ^-, which should be near zero; i.e., the atmosphere should be deep enough to fully absorb any energetic electrons generated above the lower boundary. Photoelectrons are applied at every vertical and energy grid point according to the production process described above. The transport equations are first solved at the highest energy level, and then progressively downward in energy until the lowest energy bin is reached. Each energy level generates cascade into lower energy levels through energy loss collisions; the problem of calculating this on a variable grid is solved using the bin-weighted method by *Swartz* [1985]. Each energy level also generates secondary electrons from ionizing collisions that are added to the production at lower energies; the functional form used by *Jackman et al.* [1977] is employed to calculate the secondary electron production function.

Energetic electrons undergo elastic and inelastic collisions and, in the two-stream formalism, can only be scattered backward or forward. The elastic scattering redistribution function, T_1, is

$$T_1 = \sum_i (b_i \sigma_i^e n_i) \tag{5}$$

where for every species i, b_i is the backscatter probability, σ_i^e is the elastic cross section, and n_i is the density. The loss function from each stream, T_2, is

$$T_2 = \sum_i (b_i \sigma_i^e n_i + \sigma_i^l n_i) \tag{6}$$

where σ^l is the sum of all inelastic (energy loss) processes, including energy transfer to ambient electrons [*Swartz et al.*, 1971]. Then, in simplified form, the equations for the downward and upward flux $\phi^\pm$ are

$$d\phi^-/ds = T_1\phi^+ - T_2\phi^- + Q^- + q/2 \tag{7}$$

$$d\phi^+/ds = T_1\phi^- - T_2\phi^+ + Q^+ + q/2 \tag{8}$$

where $Q^\pm$ represents the cascade and secondary production from higher energy levels, q is the photoelectron production, and all variables are implicitly functions of s. By differentiation and substitution, a second-order parabolic differential equation for the downward electron flux is obtained as follows:

$$\frac{d^2\phi^-}{ds^2} + \alpha \frac{d\phi^-}{ds} + \beta\phi^- + \gamma = 0 \tag{9}$$

where α, β, and γ are the collected terms in T_1, T_2, q, Q, and their derivatives. This equation is solved for ϕ^- using the Crank-Nicholson (tri-diagonal) method. Since the energetic electron flux is assumed to be time-independent, the steady state solution is found in one iteration. After ϕ^- is solved at all altitudes, ϕ^+ is obtained by integrating equation (8) from the bottom of the atmosphere to the top.

Excitation and ionization rates are then calculated at all altitudes, using the same cross sections embedded in the σ_i^e and T_2 terms. Elastic cross sections and backscatter ratios are interpolated from tables, and excitation and ionization cross sections are formulated from analytic functions following the *Green and Stolarski* [1972] and *Jackman et al.* [1977] methods, but with significant revisions (see Appendix A of *Solomon et al.* [1988] and section 3.2 below). Relativistic corrections to cross sections at high energy are included, so in principle the algorithm can be used for incident electrons up to 1 GeV by simply increasing the number of bins in the energy grid.

2.2.5. Chemistry

The output from the photoionization and electron transport algorithms is used as input to the chemical model, along with T_n, T_i, T_e, and, above 200 km, the electron density. The ion-neutral-metastable chemistry is solved in steady state equilibrium for the specified input conditions. The chemical rate coefficients used in the model are similar to those tabulated in *Solomon et al.* [1988], as updated by *Hill et al.* [2000] and *Bailey et al.* [2002]. However, some revisions due to newer laboratory results are indicated, as shown by *Richards* [2011]. Also see *Roble* [1995] for a description of the basic TIE-GCM ion-neutral chemistry.

For a known electron density, it is straightforward to solve for ion densities by working from high-energy ions to low. However, below 200 km, we wish to calculate the electron density in photochemical equilibrium. Previously this was accomplished using a quartic equation solution developed for use in the TIE-GCM, but inconsistent results led to the need for a more robust technique, which is described here.

A simple iterative scheme is used to solve for the electron density $[e^-]$ in the photochemical equilibrium region. An initial estimate of $[e^-]$ is made by assuming that $[e^-]$ equals the sum of the major atomic ions ($\Sigma_{ai} = O^+(^4S, {}^2D, {}^2P) + N^+$) and the major molecular ions ($\Sigma_{mi} = NO^+ + O_2^+ + N_2^+$), and that the molecular ions recombine with an effective dissociative recombination rate coefficient α_{eff}, which is estimated as the mean of the individual dissociative recombination rate coefficients. The total ionization rate I_T (including both photoionization and energetic electron impact ionization) is calculated, and, since all nearly ionization ultimately flows through the molecular ions to recombine, the ionization rate is equated with the effective recombination rate, resulting in

$$\sum_{mi} = I_T / (\alpha_{eff}[e^-]) \tag{10}$$

Applying charge neutrality,

$$[e^-] = I_T/(\alpha_{eff}[e^-]) + \sum_{ai} \qquad (11)$$

which results in a quadratic equation

$$[e^-]^2 - \sum_{ai}[e^-] - I_T/\alpha_{eff-} = 0 \qquad (12)$$

that is easily solved for $[e^-]$. This initial estimate is used to calculate all ions considering their actual rate coefficients, and then $[e^-]$ is adjusted to equal the mean of its estimated value and the sum of all ions. That value of $[e^-]$ is used to recalculate all ions, and the procedure is iterated five times. This converges very rapidly; two or three iterations would be sufficient to obtain accuracy at the ~1% level, but the extra iterations are employed to ensure convergence, since the procedure is quite computationally efficient.

There are five options for dealing with ion/electron chemistry in GLOW. The default is described above, but it is also possible to simply specify $[e^-]$ at all altitudes, and then calculate all ions, assuming charge neutrality. Another option is to specify $[e^-]$ and the major ions O^+, O_2^+, and NO^+ but calculate all minor ions, and it is also possible to specify all ions except $O^+(^2P)$ and $O^+(^2D)$, or to turn off all chemical calculations.

Once the ion chemistry is solved, the following excited neutral metastable densities are calculated, in order of descending energy: $N(^2P)$, $N(^2D)$, $N_2(A^3\Sigma)$, $O(^1S)$, and $O(^1D)$. There are a few minor feedback dependencies in this scheme, owing to reactions such as $O^+ + N(^2D)$ and electron quenching of $O^+(^2P, {}^2D)$. Therefore, the metastable and ion densities are iterated in the same loop as for the electron density described above, resulting in rapid convergence.

2.2.6. Emissions

Once all excitation rates, ion densities, and excited metastable species densities have been calculated, it is straightforward to compute the contributions to airglow emissions. Volume emission rates are first calculated for each known production mechanism of each spectral emission feature. This enables a process-specific breakdown of the emission rates for use in analysis. The individual contributions are then summed to obtain the total volume emission rates.

The emergent slant path column brightness is easily calculated for optically thin emissions by integrating through the model output fields; the vertical column brightness is provided as a standard output field for convenience. However, for emissions that are subject to absorption or scattering, and particularly for optically thick emissions, post-processing must perform radiative transfer calculations.

2.3. Implementation

The basic idea governing implementation is to provide a family of modules and subroutines that are called by a driver program, so that users can write their own driver programs to address specific problems, using the examples provided as guidance. The modular structure enables extraction of individual subroutines for other purposes. GLOW is a Fortran-90 code that is very computationally efficient; a single column executes in less than 0.1 s on a single processor, and with parallel processing the model can be run for the entire globe in seconds. An additional development goal is to provide clearly written, self-documenting software that is available to the community and the general public through an open-source academic research license. In essence, this license permits any research usage and development, but prohibits inclusion with closed-source code, and sales.

A note on units: GLOW uses cgs in its internal calculations. Wavelengths are described in nanometers in this publication, but Ångstroms are used for solar and airglow emission wavelengths inside the code. Energies are in electron volts (eV), except for the input auroral total energy flux, which is expressed in erg cm^{-2} s^{-1}. Other units employed for convenience are megabarns (10^{-18} cm^2) and Rayleighs (10^6 photons cm^{-2} s^{-1}). Conductivities are output in siemens/meter. Kilometers are used in driver program altitude grids but are converted to centimeters internally. Dates are in yyyyddd format, universal time is in seconds, and local solar time is in hours. The solar radio flux index $F_{10.7}$ is expressed in units of 10^{-22} Wm^{-2}.

2.3.1. Code Structure

An overview of the GLOW calling tree is shown in Figure 1. This figure represents a configuration using the GLOWDRIVER program, which is designed for performing calculations at all global locations, but the GLOWBASIC program, which is a serial configuration for running one column at a time, is also provided,
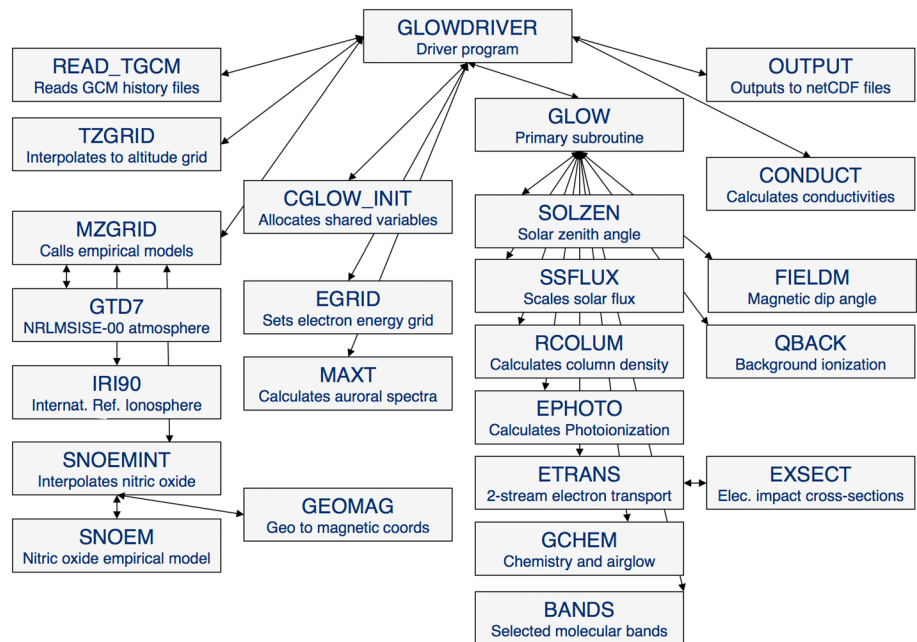
Figure 1. Schematic diagram showing the calling tree of the GLOW model when run by program GLOWDRIVER. The driver program can either obtain ambient atmosphere inputs from general circulation model history files or from empirical models, in this case, NRLMSISE-00, IRI-90, and NOEM. The driver then calls CGLOW_INIT and other setup subroutines, and calls subroutine GLOW, which handles all internal calculations. At the end of each specified time interval, the driver calls CONDUCT to calculate conductivities and outputs results to netCDF and/or text files.

similar to example driver programs provided with earlier versions. GLOWDRIVER requires MPI for parallel processing and netCDF libraries for I/O, but GLOWBASIC requires only a standard Fortran-90 compiler. Certain functions are performed through calls by the driver program(s), such as specification of the energy grid, and calculation of conductivities using the algorithm from *McGranaghan et al.* [2015a,b], but most functionality is provided through calls by subroutine GLOW, the eponymous master routine of the model. GLOW initializes module CGLOW, which defines shared variables, replacing the functionality previously provided through a common block of the same name. Any variable defined in cglow can be use-associated to driver programs for output.

2.3.2. Parallel Processing
Parallel processing is implemented with a standard message-passing-interface (MPI) library through domain-decomposition in latitude. It is configurable to any number of processors that is an integral factor of the number of latitudes. All MPI calls are handled by GLOWDRIVER, which obtains inputs through the master task, distributes latitude bands to the other tasks, and collects results for output. When running with heritage empirical models that are not parallelizable due to their code structure, the master task performs all empirical model calls before distribution of ambient fields to the other tasks.

2.3.3. Input/Output
Input specifications for GLOWDRIVER are read from a namelist input file; examples are provided in the standard distribution. GCM history file input is performed using the netCDF library, as is global output, essentially mimicking the TIE-GCM history file format. Diagnostic text to standard output is also provided, and code can easily be added to output text fields to specified files. When running the GLOWBASIC driver, input parameters are obtained through a simple ASCII specification list on standard input, and columnar output is written to standard output. This is of course configurable by simple edits to the driver program.

2.3.4. Additional Information
The GLOW code can be obtained at https://www2.hao.ucar.edu/modeling/glow and at https://github.com/NCAR/GLOW. Several documents included with the code provide more detailed information and instruction. These include a "quickstart" file, release notes, a license file, and the primary documentation file *Glow.txt*. Source code files also contain many variable definitions in their headers. The standard distribution is a

fairly flat directory structure but does include a/data subdirectory where input data files are located, including data files for the IRI model.

2.4. Outputs

Table 1 contains a summary of model inputs and outputs. Note that the input state variables are also passed through to output. In the cases of [e$^-$] and N(^{2}D), that means that there are two output fields, one for the initial values and one for the values calculated by GLOW. Airglow emission features have been added over the years and hence are in no particular order in the output array; additional features are added periodically. For molecular bands, some are specific vibrational bands and others are integrated over the band system. Production rate arrays derived from the electron transport algorithm generally refer to total band system excitation for molecules and total multiplet excitation for atomic oxygen. Band systems may be apportioned to individual upper states using Franck-Condon factors or collisional algorithms, a subroutine under development that provides a simple upper state distribution, currently only for the LBH band system. Any rate or field array that is available through module CGLOW can be added to driver programs as use-associated variables and added to output.

Post-processing programs for use with these outputs are also available. Examples include vibrational-rotational band models, radiative transfer algorithms, global line-of-sight geometry, and graphical display. These are not formally part of the GLOW model but are used in the example results shown below.

3. Results

3.1. Example Results

3.1.1. Dayglow

Example results for a typical dayglow case are shown in Figure 2. This is a single-column simulation for local noon at 40° north latitude, 105° west longitude, at the vernal equinox, for low, medium, and high solar activities. Empirical model inputs from NRLMSISE-00, IRI-90, and NOEM were employed using the GLOWBASIC driver program. Total ionization rates, ion densities, and selected volume emission rates are plotted, including the N$_2$ 1N(0,1) band at 427.8 nm, the O(^{1}S) line at 557.7 nm, the O(^{1}D) line at 630.0 nm, the O(3p^{3}P) line at 844.6 nm, the N$_2$ LBH "shortwave" bands (141–153 nm), the O(3s^{5}S) doublet at 135.6 nm, and the N(3s^{2}P) doublet at 149.3 nm. Note that the 149.3 nm doublet is speculative until it is compared with well-calibrated observations; it is included here with a source from dissociative photoionization because it falls within the LBH shortwave bands observed by TIMED/Global Ultraviolet Imager (GUVI) and other space-based imagers.

3.1.2. Aurora

Example results for auroral cases are shown in Figure 3, using the same methods and format as Figure 2, for energy flux of 2 mW/m^2 and characteristic energies of 1, 2, and 5 keV. The geophysical conditions were local midnight at 60° north latitude, 105° west longitude, vernal equinox, $F_{10.7}$ = 130.

3.1.3. Nightglow

Thermospheric nightglow features hardly need the power of the GLOW model, since there are no photons or electrons to transport, and the remaining excitation processes stem from recombination of the F region ionosphere. This results in, for example, O(1D), O(1S), and N(2D), resulting in 630.0, 557.7, and 520.0 nm emissions. There are many other important airglow emissions in the mesopause region ~85 to ~100 km, which will be included in future versions of GLOW, but currently the model region of validity does not extend below ~100 km. There are also O$^+$ radiative recombination features, which are useful for remote sensing of the night ionosphere from space. The 135.6 nm recombination source is included in the far ultraviolet simulations shown in Figure 4.

3.2. Far Ultraviolet Airglow

3.2.1. Global Simulations

One motivation for release of this version of GLOW is to prepare for observations by the NASA Global-scale Observations of the Limb and Disk (GOLD) mission [*Eastes et al.*, 2008], a far ultraviolet imager that will be launched in 2018 to geostationary orbit at 47.5° west longitude. The O(^{5}S) doublet at 135.6 nm and the N$_2$ LBH bands will be used to remotely sense thermospheric composition (column O/N$_2$ ratio) and temperature (through the rotational structure of the LBH bands). This requires radiative transfer calculations for the O emissions and vibrational-rotational band model simulations for the LBH bands. These are handled in post-processing, along with line-of-sight integrations, and will be described in subsequent publications. For
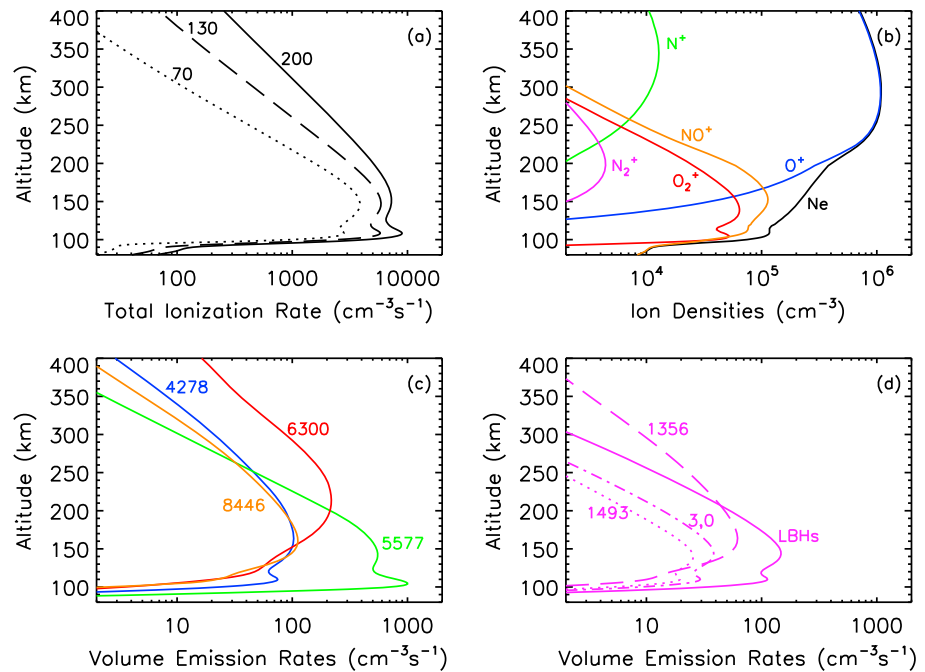
Figure 2. Example output from the GLOW model for daytime conditions—local noon at 40° north latitude, 105° west longitude, on 21 March. An empirical atmosphere specified by MSIS/IRI/NOEM was employed. (a) Total ionization rate for solar maximum ($F_{10.7} = 200$, solid line), solar medium ($F_{10.7} = 130$, dashed line), and solar minimum ($F_{10.7} = 70$, dotted line) conditions. (b) Ion densities for solar medium conditions, as labeled. (c) Volume emission rates of selected visible and near-IR emission features. Blue: N_2 1N band at 427.8 nm, green: $O(^1S)$ line at 557.7 nm, red: $O(^1D)$ line at 630.0 nm, orange: $O(3p^3P)$ line at 844.6 nm. The double-peak structure in the 557.7 nm emission is caused by overlapping production mechanisms, $N_2(A) + O$ at higher altitude and O_2 photodissociation at lower altitude. (d) Volume emission rates of selected UV features. Solid line: N_2 LBH "shortwave" bands (141–153 nm). Dot-dashed line: LBH (3,0) band at 135.4 nm. Dashed line: $O(3s^5S)$ doublet at 135.6 nm. Dotted line: $N(3s^2P)$ doublet at 149.3 nm. Note that the 149.3 nm doublet is speculative until it is compared with well-calibrated observations.

135.6 nm, radiative transfer is fairly simple, and has a small effect on results; by contrast, the optically thick triplet at 130.4 nm requires sophisticated treatment, for example, using the partial-frequency-redistribution method of *Gladstone* [1988]. Figure 4 shows an example simulation of GOLD observations. Dayglow, nightglow, and auroral emissions are included, on the disk and on the limb, demonstrating the versatility of the simulation method.

3.2.2. Comparison With Observations by TIMED/GUVI

For initial validation of the far ultraviolet airglow simulations, simulations are compared to measurements by the Global Ultraviolet Imager (GUVI) instrument on the TIMED spacecraft [*Christensen et al.*, 2003]. The data are level 2b limb scans of the $O(^5S)$ emission at 135.6 nm and LBH shortwave emission at 141–153 nm obtained from R. R. Meier [*Meier et al.*, 2015]. The plots shown in Figure 5 are of daily zonal means at low to middle latitude (±45°), averaged into six 15° latitude bands, color coded with the mean latitude and solar zenith angle at the tangent point indicated. Two days are shown as examples: day 80 of 2002 during moderately high solar activity ($F_{10.7} = 174$, $<F_{10.7}> = 189$) and day 65 of 2007 during moderately low solar activity, ($F_{10.7} = 72$, $<F_{10.7}> = 75$). The model was run with basic EUVAC, NRLMSISE-00, and IRI-90 inputs, with no attempt to adjust the O/N_2 ratios, so close correspondence is not expected in all cases. The model limb brightnesses were obtained from volume emission rates by integrating along a virtual slant path through a single model column located at the tangent point; this is an acceptable approximation for solar zenith angles $<\sim70°$ [*Meier et al.*, 2015]. Radiative transfer effects for the 135.6 nm emission and absorption by O_2 for the LBH emission were included. The (3,0) LBH band at 135.4 nm is included in the 135.6 simulation, and the N$(3s^2P)$ doublet at 149.3 nm is included in the LBH simulation. The entire GUVI limb scan database was run from early 2002 to mid-2007. Agreement was excellent with regard to the height of both emission peaks and very good with regard to the shape of the profiles and their dependence on solar zenith angle. The model tends to overestimate the absolute magnitude of emission rates at high solar activity and
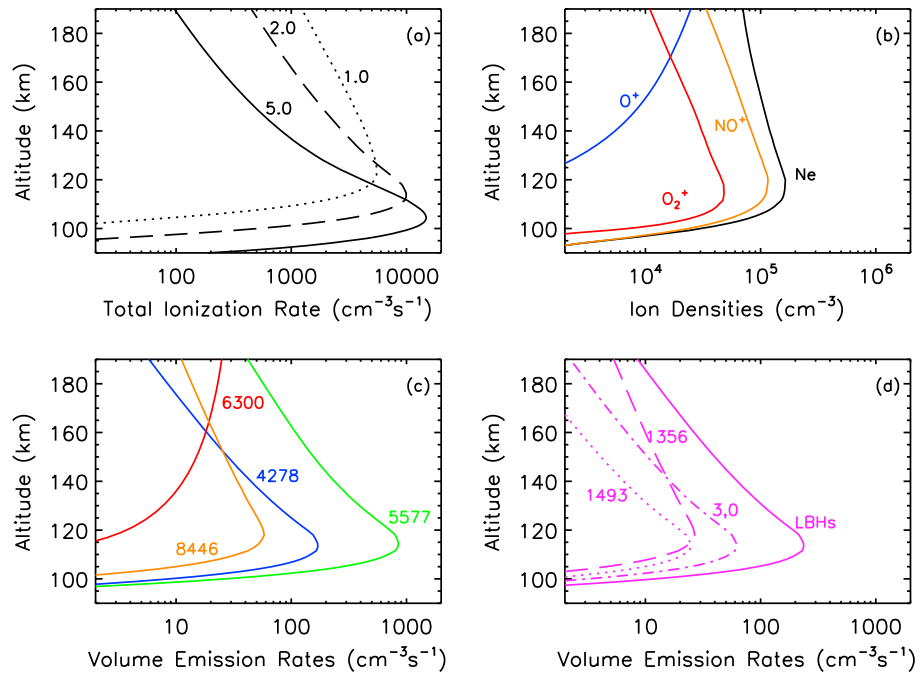
Figure 3. Example output from the GLOW model for auroral conditions at moderate solar activity—local midnight at 60° north latitude, 105° west longitude, on 21 March. An empirical atmosphere specified by MSIS/IRI/NOEM was employed. (a) Total ionization rate for 2.0 mW/m^2 Maxwellian input spectra with characteristic energy of 5.0 keV (solid line), 2.0 keV (dashed line), and 1.0 keV (dotted line). (b) Ion densities for the 2 keV case, as labeled. (c) Volume emission rates of selected visible and near-IR emission features for the 2 keV case, as in Figure 2. (d) Volume emission rates of selected UV features for the 2 keV case, as in Figure 2.

underestimate them at low solar activity, possibly indicating too much solar cycle variability in the EUVAC model, if the GUVI calibration is stable.

The difficulties of aligning the cross sections used in models with airglow observations are well known (see the extensive discussion by *Meier et al.* [2015]). Here the LBH total band system cross section is scaled from the sum of the N$_2$ (*a*,*a'*,*w*) singlets by a factor of 0.7 to account for partial cascade. The excitation cross sections were originally adapted from *Cartwright et al.* [1977], and the scaling employed results in
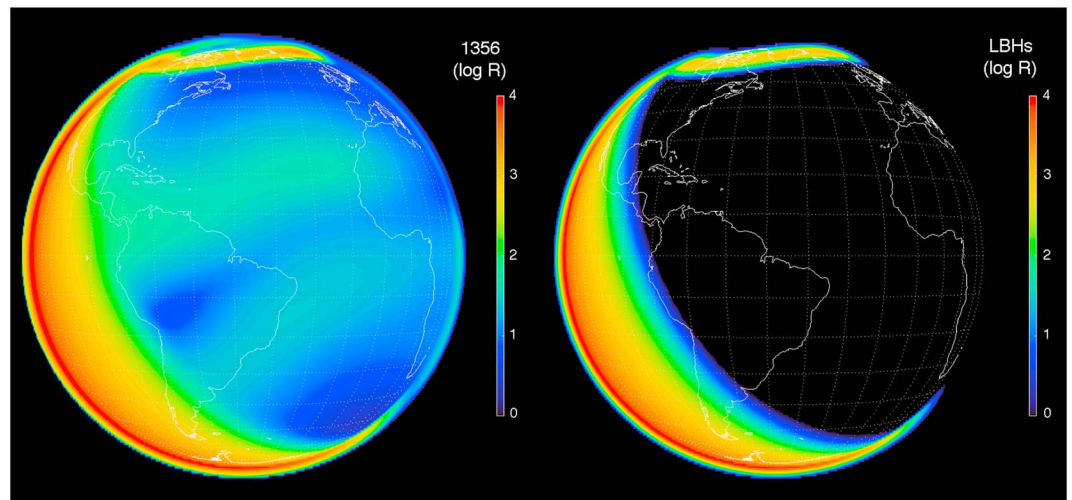

Figure 4. Synthetic global images generated by the TIE-GCM and GLOW models for an instrument located at geostationary orbit (6.6 R_E above the center of the Earth) at 47.5° west longitude, at 0 UT during southern hemisphere summer solstice and high solar activity. (left) The O(^{5}S) doublet at 135.6 nm (including the underlying LBH (3,0) band). (right) LBH emissions in the 141–153 nm range.
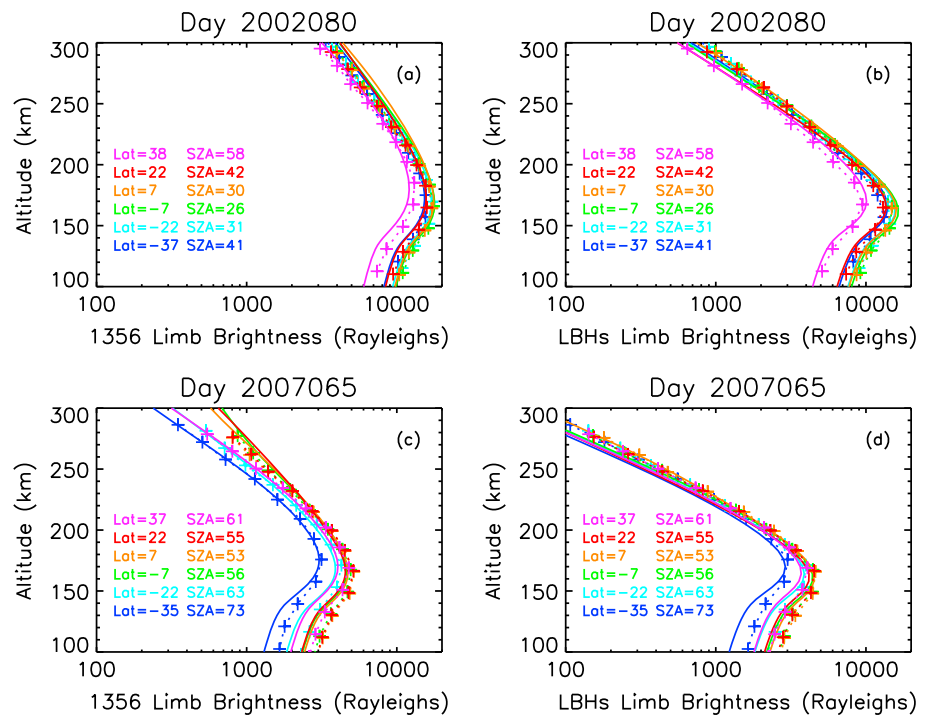
Figure 5. Comparison of GLOW limb scan simulations to measurements by the GUVI instrument on the TIMED satellite. The plots shown are daily zonal means at low to middle latitude (±45°), averaged into six 15° latitude bands, as color coded with the mean latitude and solar zenith angle at the tangent point indicated. Solid lines—model simulations. Dotted lines with plusses—measurements. (a and c) $O(^5S)$ emission at 135.6 nm. (b and d) LBH "shortwave" emission at 141–153 nm. (a and b) Day 80 of 2002 during moderately high solar activity, $F_{10.7} = 174$, $\langle F_{10.7} \rangle = 189$. (c and d) Day 65 of 2007 during moderately low solar activity, $F_{10.7} = 72$, $\langle F_{10.7} \rangle = 75$.

reasonable correspondence with *Ajello et al.* [2010]. This results in a peak total cross section value of 3.0×10^{-17} cm^2 (before 13% loss to predissociation), compared to 4.0×10^{-17} cm^2 used by *Meier et al.* [2015]. Frank-Condon factors from *Ajello and Shemansky* [1985] were employed. For 135.6 nm, the primary source of uncertainty is cascade to $O(^5S)$ through the $O(3p^5P)$ state, which results in 777.4 nm emission. The effective 777.4 nm cross section was scaled to a peak value of 3.4×10^{-18} cm^2, resulting in a total emission cross section for 135.6 nm that peaks at 6.5×10^{-18} cm^2, compared to 8.6×10^{-18} cm^2 from *Meier et al.* [2015]. As noted above, uncertainties in the solar EUV irradiance and its variability, particularly in the soft X-ray region, are convolved with these issues. We have some evidence of convergence of various model simulations with actual observations, but these model calibration issues imply that O/N_2 obtained from remote sensing observations is a relative quantity.

4. Discussion

4.1. Strengths

GLOW is a fast, parallel, model, with a modular structure of available open-source code, written in standard Fortran-90, that is readily ported to any computer from single processors to supercomputers. It is easy to use—although designed for program interfaces written by the user, it can also be run using the example drivers with no particular knowledge of programming languages. It is flexible with regard to adaptation for aurora and/or photoelectron cases, individually, combined, or for other purposes. It is intended to be a readable code with extensive in-line definition and explanation. It is documented through this paper, combined with the references cited, the file Glow.txt, and release notes. The heritage of the two-stream Nagy/Banks code is maintained in a modern programming structure; this proven algorithm is an effective and efficient method for electron transport calculations. In combination with a general circulation model such as the TIE-GCM, and post-processing by band model and radiative transfer calculations, it provides a powerful tool for thermosphere/ionosphere simulation and analysis. It has full metastable ion-neutral chemistry, including,

e.g., N(^{2}P), which is often neglected in similar calculations. Chemical rate coefficients, branching ratios, and transition coefficients, are easily configurable.

4.2. Limitations

Since GLOW is a single-column model, and assumes a single solar zenith angle and magnetic dip angle throughout the column, horizontal gradients and transport are neglected. Results near the magnetic equator should thus be used with caution. It is also a time-independent formulation, which is adequate for fast ion-neutral chemistry in the thermosphere, but in the E region at low altitude, ion lifetimes can become longer during sunset. The lack of dynamical and electrodynamical transport is remedied by using GCM output. The range of validity of the model is ~100 to ~600 km. At lower altitudes, although the electron transport works, there is no odd-oxygen or odd-hydrogen chemistry and hence no neutral recombination airglow features such as O_2 atmospheric bands and OH Meinel bands. At higher altitudes, the lack of H, He, and their ions means that the code cannot be used in the plasmasphere without modification.

The two-stream electron transport method is a "collisional" code that neglects magnetic mirroring and any other electromagnetic effects, including wave-particle interactions. It is not appropriate for fluxes that have highly anisotropic pitch angles in the downward direction. It is only strictly valid for pitch angles of ±60°, but has been shown to be a good approximation for isotropic auroral distributions [e.g., *Solomon*, 2001], and for photoelectrons. The magnetic field model currently employed is highly simplified and has no secular evolution; it is adequate for the auroral region but should be upgraded to the IGRF standard to accurately conduct, e.g., conjugate photoelectron studies.

Other issues with the model as currently implemented are not so much inherent limitations as areas where additional work is needed, as described below.

4.3. Future Development

The lack of mesopause-region chemistry and recombination emissions is particularly important for O(^{1}S) emissions, since the well-known 557.7 nm "green line" is nominally in the model, but does not include the atomic oxygen recombination source that is prominent at night. O_2 atmospheric, IR atmospheric, and Hertzberg bands will also be added. Other emissions that need to be reexamined include the 777.4 nm cascade to O(^{5}S), and the N(3s^{2}P) 149.3 nm doublet, as discussed in section 3.2.2 above. Evaluation and updating of ion chemistry [cf., *Richards*, 2011] should also be done, and addition of H and He neutral fields to facilitate inclusion of H$^+$ and He$^+$ chemistry. Addition of an option for specifying ionization due to auroral proton precipitation is in progress.

Another priority for development is to reevaluate electron impact cross sections, break out the several lumped states (N_2 triplets, N_2 singlets, O_2 Hertzbergs, etc.), and introduce cascade and thresholding effects for, in particular, LBH vibrational states. Electron cross sections will have a more flexible specification methodology, tabular input files instead of in-line analytic functions.

An ongoing issue is obtaining correct inputs for ionizing solar radiation, particularly in the soft X-ray to hard EUV region ~1 to ~25 nm. New data and models derived from SDO/EVE and the Miniature X-ray Solar Spectrometer CubeSat [*Woods et al.*, 2011, 2017] will be of value here, but need to be codified for model input. Another detail in this area is implementing a day-of-year correction for the Sun-Earth distance.

Finally, interfaces to additional GCMs will be provided. Most important of these is an interface to the Whole Atmosphere Community Climate Model–eXtended (WACCM-X) [*Liu et al.*, 2010], which now includes a fully interactive ionosphere and electrodynamo. This will facilitate mesopause-region chemistry development, since WACCM-X already contains a sophisticated treatment. An interface with WACCM-X will extend model simulations of the effects of lower atmosphere weather on space weather to include airglow diagnostics.

References

Ajello, J. M., and D. E. Shemansky (1985), A reexamination of important N_2 cross sections by electron impact with application to the dayglow: The Lyman-Birge-Hopfield band system and NI (119.99 nm), *J. Geophys. Res.*, *90*, 9845–9861, doi:10.1029/JA090iA10p09845.

Ajello, J. M., R. S. Mangina, and R. R. Meier (2010), UV molecular spectroscopy from electron impact for applications to planetary astronomy and astrophysics, in *Charged Particle and Photon Interactions With Matter, Recent Advances, Applications, and Interfaces*, edited by Y. Hatano, Y. Katsumura, and A. Mozumder, pp. 761–804, Taylor and Francis, Boca Raton, Fla.

Bailey, S. M., C. A. Barth, and S.C. Solomon (2002), A model of nitric oxide in the lower thermosphere, *J. Geophys. Res.*, *107*(A8), 1205, doi:10.1029/2001JA000258.

Banks, P. M., and A. F. Nagy (1970), Concerning the influence of elastic scattering upon photoelectron transport and escape, *J. Geophys. Res.*, *75*, 1902–1910, doi:10.1029/JA075i010p01902.

Banks, P. M., C. R. Chappell, and A. F. Nagy (1974), A new model for the interaction of auroral electrons with the thermosphere: Spectral degradation, backscatter, optical emission, and ionization, *J. Geophys. Res.*, *79*, 1459–1470, doi:10.1029/JA079i010p01459.

Barth, C. A., K. D. Mankoff, S. M. Bailey, and S. C. Solomon (2003), Global observations of nitric oxide in the thermosphere, *J. Geophys. Res.*, *108*(A1), 1027, doi:10.1029/2002JA009458.

Bilitza, D. (1990), International Reference Ionosphere: IRI-90, pp. 90–22, Natl. Space Sci. Data Cent. Rep., Greenbelt, Md. [Available at https://ntrs.nasa.gov/archive/nasa/casi.ntrs.nasa.gov/19910021307.pdf.]

Buonsanto, M. J., S. C. Solomon, and W. K. Tobiska (1992), Comparison of measured and modeled solar EUV flux and its effect on the E–F_1 region ionosphere, *J. Geophys. Res.*, *97*, 10,513–10,524, doi:10.1029/92JA00792.

Buonsanto, M. J., P. G. Richards, W. K. Tobiska, S. C. Solomon, Y.-K. Tung, and J. A. Fennelly (1995), Ionospheric electron densities calculated using different EUV flux models and cross sections: Comparison with radar data, *J. Geophys. Res.*, *100*, 14,569–14,580, doi:10.1029/95JA00680.

Cartwright, D. C., A. Chutjian, S. Trajmar, and W. Williams (1977), Electron impact excitation of the electronic states of N_2, 2, integral cross sections at incident energies from 10 to 50 eV, *Phys. Rev. A*, *16*, 1041, doi:10.1103/PhysRevA.16.1041.

Chapman, S. (1931), The absorption and dissociative or ionizing effect of monochromatic radiation in an atmosphere on a rotating Earth, part II, grazing incidence, *Proc. Phys. Soc.*, *43*, 483.

Christensen, A. B., et al. (2003), Initial observations with the Global Ultraviolet Imager (GUVI) in the NASA TIMED satellite mission, *J. Geophys. Res.*, *108*(A12), 1451, doi:10.1029/2003JA009918.

Conway, R. R. (1988), Photoabsorption and photoionization cross section of O, O_2, and N_2 for photoelectron production calculations: A compilation of recent laboratory measurements, *NRL Mem. Rep. 6155*, Nav. Res. Lab., Washington, D. C.

Doe, R. A., J. P. Thayer, and S. C. Solomon (2005), Incoherent scatter radar measurements and modeling of high-latitude solar photoionization, *J. Geophys. Res.*, *110*, A10303, doi:10.1029/2005JA011129.

Eastes, R. W., et al. (2008), Global-scale observations of the limb and disk (GOLD): New observing capabilities for the ionosphere-thermosphere, in *Midlatitude Ionospheric Dynamics and Disturbances*, *Geophys. Monogr. Ser.*, vol. 181, edited by P. M. Kintner et al., pp. 319–326, AGU, Washington, D. C.

Fang, X., D. Lummerzheim, and C. H. Jackman (2013), Proton impact ionization and a fast calculation method, *J. Geophys. Res. Space Physics*, *118*, 5369, doi:10.1002/jgra.50484.

Fennelly, J. A., and D. G. Torr (1992), Photoionization and photoabsorption cross sections of O, N_2, O_2, and N for aeronomic calculations, *At. Data Nucl. Data Tables*, *51*, 321.

Gladstone, G. R. (1988), UV resonance line dayglow emissions on Earth and Jupiter, *J. Geophys. Res.*, *93*, 14,623–14,630, doi:10.1029/JA093iA12p14623.

Green, A. E. S., and R. S. Stolarski (1972), Analytic models of electron impact excitation cross sections, *J. Atmos. Terr. Phys.*, *34*, 1703.

Henke, B. L., E. M. Gullikson, and J. C. Davis (1993), X-ray interactions—Photoabsorption, scattering, transmission, and reflection at $E = 50$–30,000 eV, $Z = 1$–92, *At. Data Nucl. Data Tables*, *54*, 181.

Hill, S. M., S. C. Solomon, D. D. Cleary, and A. L. Broadfoot (2000), Temperature dependence of the reaction $N_2(A^3\Sigma_u^+) + O$ in the terrestrial thermosphere, *J. Geophys. Res.*, *105*(A5), 10,615–10,629.

Hinteregger, H. E., K. Fukui, and B. R. Gilson (1981), Observational, reference, and model data on solar EUV, from measurements on AE–E, *Geophys. Res. Lett.*, *8*, 1147–1150, doi:10.1029/GL008i011p01147.

Jackman, C. H., R. H. Garvey, and A. E. S. Green (1977), Electron impact on atmospheric gases, 1, updated cross sections, *J. Geophys. Res.*, *82*, 5081–5090, doi:10.1029/JA082i032p05081.

Kaeppler, S. R., D. L. Hampton, M. J. Nicolls, A. Stromme, S. C. Solomon, J. H. Hecht, and M. G. Conde (2015), An investigation comparing ground-based techniques that quantify auroral electron flux and conductance, *J. Geophys. Res. Space Physics*, *120*, 9038–9056, doi:10.1002/2015JA021396.

Liu, H.-L., et al. (2010), Thermosphere extension of the Whole Atmosphere Community Climate Model, *J. Geophys. Res.*, *115*, A12302, doi:10.1029/2010JA015586.

Marsh, D. R., S. C. Solomon, and A. E. Reynolds (2004), Empirical model of nitric oxide in the lower thermosphere, *J. Geophys. Res.*, *109*, A07301, doi:10.1029/2003JA010199.

Meier, R. R., D. J. Strickland, J. H. Hecht, and A. B. Christensen (1989), Deducing composition and incident electron spectra from ground-based auroral optical measurements: A study of auroral red line processes, *J. Geophys. Res.*, *94*, 13,541–13,552, doi:10.1029/JA094iA10p13541.

Meier, R. R., et al. (2015), Remote sensing of Earth's limb by TIMED/GUVI: Retrieval of thermospheric composition and temperature, *Earth Space Sci.*, *2*, 1, doi:10.1002/2014EA000035.

McGranaghan, R., D. J. Knipp, S. C. Solomon, and X. Fang (2015a), A fast, parameterized model of upper atmospheric ionization rates, chemistry, and conductivity, *J. Geophys. Res. Space Physics*, *120*, 4936–4949, doi:10.1002/2015JA021146.

McGranaghan, R., D. J. Knipp, T. Matsuo, H. Godinez, R. J. Redmon, S. C. Solomon, and S. K. Morley (2015b), Modes of high-latitude auroral conductance variability derived from DMSP energetic electron precipitation observations: Empirical orthogonal function analysis, *J. Geophys. Res. Space Physics*, *120*, 11,013–11,031, doi:10.1002/2015JA021828.

Nagy, A. F., and P. M. Banks (1970), Photoelectron fluxes in the ionosphere, *J. Geophys. Res.*, *75*, 6260–6270, doi:10.1029/JA075i031p06260.

Peterson, W. K., E. N. Stavros, P. G. Richards, P. C. Chamberlin, T. N. Woods, S. M. Bailey, and S. C. Solomon (2009), Photoelectrons as a tool to evaluate spectral variations in solar EUV irradiance over solar cycle time scales, *J. Geophys. Res.*, *114*, A10304, doi:10.1029/2009JA014362.

Peterson, W. K., T. N. Woods, J. M. Fontenla, P. G. Richards, P. C. Chamberlin, S. C. Solomon, W. K. Tobiska, and H. P. Warren (2012), Solar EUV and XUV energy input to thermosphere on solar rotation time scales derived from photoelectron observations, *J. Geophys. Res.*, *117*, A05320, doi:10.1029/2011JA017382.

Picone, J. M., A. E. Hedin, D. P. Drob, and A. C. Aikin (2002), NRLMSISE-00 empirical model of the atmosphere: Statistical comparisons and scientific issues, *J. Geophys. Res.*, *107*(A12), 1468, doi:10.1029/2002JA009430.

Qian, L., A. G. Burns, B. A. Emery, B. Foster, G. Lu, A. Maute, A. D. Richmond, R. G. Roble, S. C. Solomon, and W. Wang (2014), The NCAR TIE-GCM: A community model of the coupled thermosphere/ionosphere system, in *Modeling the Ionosphere-Thermosphere System*, *Geophys. Monogr. Ser.*, vol. 201, edited by J. Huba, R. Schunk, and G. Khazanov, pp. 73–83, AGU, Washington, D. C., doi:10.1002/9781118704417.ch7.

Richards, P. G. (2011), Reexamination of ionospheric photochemistry, *J. Geophys. Res.*, *116*, A08307, doi:10.1029/2011JA016613.

Richards, P. G., J. A. Fennelly, and D. G. Torr (1994), EUVAC: A solar EUV flux model for aeronomic calculations, *J. Geophys. Res.*, *99*, 8981–8992, doi:10.1029/94JA00518.

Richards, P. G., T. N. Woods, and W. K. Peterson (2006), HEUVAC: A new high resolution solar EUV proxy model, *Adv. Space Res.*, *37*, 315–322, doi:10.1016/j.asr.2005.06.031.

Richmond, A. D., E. C. Ridley, and R. G. Roble (1992), A thermosphere/ionosphere general circulation model with coupled electrodynamics, *Geophys. Res. Lett.*, *19*, 601–604, doi:10.1029/92GL00401.

Roble, R. G., and E. C. Ridley (1994), Thermosphere-ionosphere-mesosphere-electrodynamics general circulation model (TIME-GCM): Equinox solar min simulations, 30–500 km, *Geophys. Res. Lett.*, *21*, 417–420, doi:10.1029/93GL03391.

Roble, R. G. (1995), Energetics of the Mesosphere and Thermosphere, in *The Upper Mesosphere and Lower Thermosphere: A Review of Experiment and Theory*, edited by R. M. Johnson and T. L. Killeen, AGU, Washington, D. C., doi:10.1029/GM087p0001.

Roble, R. G., E. C. Ridley, A. D. Richmond, and R. E. Dickinson (1988), A coupled thermosphere/ionosphere general circulation model, *Geophys. Res. Lett.*, *15*, 1325–1328, doi:10.1029/GL015i012p01325.

Smith, F. L., and C. Smith (1972), Numerical evaluation of Chapman's grazing incidence integral Ch(x,χ), *J. Geophys. Res.*, *77*, 3592–3597, doi:10.1029/JA077i019p03592.

Smithtro, C. G., and S. C. Solomon (2008), An improved parameterization of thermal electron heating by photoelectrons, with application to an X17 flare, *J. Geophys. Res.*, *113*, A08307, doi:10.1029/2008JA013077.

Solomon, S. C. (1987), Tomographic inversion of auroral emissions, PhD thesis, Univ. of Michigan, Ann Arbor Mich.

Solomon, S. C. (2001), Auroral particle transport using Monte Carlo and hybrid methods, *J. Geophys. Res.*, *106*, 107–116, doi:10.1029/2000JA002011.

Solomon, S. C. (2006), Numerical models of the *E*-region ionosphere, *Adv. Space Res.*, *37*, 1031–1037, doi:10.1016/j.asr.2005.09.040.

Solomon, S. C., and V. J. Abreu (1989), The 630 nm dayglow, *J. Geophys. Res.*, *94*, 6817–6824, doi:10.1029/JA094iA06p06817.

Solomon, S. C., and L. Qian (2005), Solar extreme-ultraviolet irradiance for general circulation models, *J. Geophys. Res.*, *110*, A10306, doi:10.1029/2005JA011160.

Solomon, S. C., P. B. Hays, and V. J. Abreu (1988), The auroral 6300 Å emission: Observations and modeling, *J. Geophys. Res.*, *93*, 9867–9882, doi:10.1029/JA093iA09p09867.

Solomon, S. C., S. M. Bailey, T. E. Holden, D. C. O'Connor, J. P. Perich, M. A. Salada, G. Stafford, K. Taylor, J. E. Vian, and P. R. Withnell (1996), The Student Nitric Oxide Explorer, *Proc. SPIE*, *2810*, 121–132, doi:10.1117/12.255131.

Solomon, S. C., S. M. Bailey, and T. N. Woods (2001), Effect of solar soft X-rays on the lower ionosphere, *Geophys. Res. Lett.*, *28*, 2149–2152, doi:10.1029/2001GL012866.

Solomon, S. C., A. G. Burns, B. A. Emery, M. G. Mlynczak, L. Qian, W. Wang, D. R. Weimer, and M. Wiltberger (2012), Modeling studies of the impact of high-speed streams and co-rotating interaction regions on the thermosphere-ionosphere, *J. Geophys. Res.*, *117*, A00L11, doi:10.1029/2011JA017417.

Swartz, W. E. (1985), Optimization of energetic electron energy degradation calculations, *J. Geophys. Res.*, *90*, 6587–6593, doi:10.1029/JA090iA07p06587.

Swartz, W. E., J. S. Nesbet, and A. E. S. Green (1971), Analytical expression for the energy transfer rate from photoelectrons to thermal electrons, *J. Geophys. Res.*, *76*, 8425, doi:10.1029/JA076i034p08425.

Tian, F., S. C. Solomon, L. Qian, J. Lei, and R. G. Roble (2008), Hydrodynamic planetary thermosphere model, II: Coupling of energetic electron transport model, *J. Geophys. Res.*, *113*, E07005, doi:10.1029/2007JE003043.

Woods, T. N., and G. J. Rottman (2002), Solar ultraviolet variability overtime periods of aeronomic interest, in *Atmospheres in the Solar System: Comparative Aeronomy*, *Geophys. Monogr. Ser.*, vol. 130, edited by M. Mendillo, A. Nagy, and J. H. Waite Jr., pp. 221–233, AGU, Washington, D. C.

Woods, T. N., F. G. Eparvier, S. M. Bailey, P. C. Chamberlin, J. Lean, G. J. Rottman, S. C. Solomon, W. K. Tobiska, and D. L. Woodraska (2005), Solar EUV Experiment (SEE): Mission overview and first results, *J. Geophys. Res.*, *110*, A01312, doi:10.1029/2004JA010765.

Woods, T. N., et al. (2011), Extreme Ultraviolet Variability Experiment (EVE) on the Solar Dynamics Observatory (SDO): Overview of science objectives, instrument design, data products, and model developments, *Sol. Phys.*, *275*, 115–143, doi:10.1007/s11207-009-9487-6.

Woods, T. N., et al. (2017), New solar irradiance measurements from the Miniature X-ray Solar Spectrometer CubeSat, *Astrophys. J.*, *835*, 122, doi:10.3847/1538-4357/835/2/122.